Spatially resolved acoustic spectroscopy for texture imaging in powder bed fusion nickel superalloys

Paul Dryburgh, Rikesh Patel, Don M. Pieris, Matthias Hirsch, Wenqi Li, Steve D. Sharples, Richard J. Smith, Adam T. Clare, and Matt Clark

View Online   Export Citation

ARTICLES YOU MAY BE INTERESTED IN

Spatially Resolved Acoustic Spectroscopy for Texture Imaging in Powder Bed Fusion Nickel Superalloys

Paul Dryburgh*, Rikesh Patel, Don M. Pieris, Matthias Hirsch, Wenqi Li, Steve D. Sharples, Richard J. Smith, Adam T. Clare, Matt Clark.

Optics and Photonics Group, University of Nottingham, University Park, Nottingham, NG7 2RD, UK.

*Corresponding author: paul.dryburgh@nottingham.ac.uk

Abstract. There is a clear industrial pull to fabricate high value components using premium high temperature aerospace materials by additive manufacturing. Inconveniently, the same material properties which allow them to perform well in service render them difficult to process via powder bed fusion. Current build systems are characterised by high defect rates and erratic microstructure, leading to components with inferior mechanical properties. The work presents microstructural texture imaging of powder-bed fusion components by a non-contact laser ultrasonic method, Spatially Resolved Acoustic Spectroscopy (SRAS). In short, this work demonstrates the ability to SRAS to detect and characterise meso-scale crystalline texture features. Probing samples manufactured by powder bed fusion, in the common nickel based aerospace superalloy Inconel 718, it has been shown the the primary crystalline orientation of can be inferred from the measured velocity, with good agreement with Electron Backscatter Diffraction. The studied sample was found to have a microstructure formation that bore a heavy resemblance to the chosen scanning pattern, with clear influence from the geometry through varying scan vector length and island-boundary scan strategy. This work forms part of a progression towards deployment of a SRAS system as an in-situ inspection solution for PBF.

INTRODUCTION

Additive Manufacturing (AM) promises to herald a new age in design flexibility by removing many traditional constraints imposed in subtractive manufacture. A specific form of AM, Powder Bed Fusion (PBF) refers to the use a high power - hundreds to thousands of Watts, to selectively irradiate a bed of metallic powder feedstock to fabricate free-form structures. The process is shown in detail in Figure 1a, where the build laser is seen to locally melt the power feedstock to create the cross-section for that layer, before the re-coater blade applies a layer of virgin power and the process repeats, in essence building parts layer-by-layer. This makes PBF well suited to creating parts with complex geometry and internal features. A detailed illustration of the melt pool zone is given in Figure 1b, highlighting distinctive features of PBF, such as strong columnar grain growth [1].

For PBF to revolutionise high-value manufacture, the development of complimentary quality control techniques is required. Current-class build systems are characterised by erratic print quality of part in the as-deposited state, namely the presence of mechanical defects and variable crystalline microstructure. Exhaustive studies on the formation mechanism of defects in PBF parts are summarised in prior work [2], in summary lack of fusion, gas porosity and cracking all plague builds and play a significant role in functional aspects such as fatigue life of PBF components. Additionally, it has been shown that even small variations in the processing parameters [3], feedstock composition [4] or part geometry [5] can lead to significant changes in the final microstructure observed. This fallibility has been a principal cause for the slow uptake of PBF in high-value industries. The high costs of both raw materials and build systems in PBF amalgamate to further punish unsuccessful builds [6]. Undertaking in-line geometrical measurements, condition monitoring and intra layer integrity evaluation are therefore key aspects for pushing AM forward and assuring that parts are of the required quality in near real-time [7].

The layer-by-layer nature of PBF presents a new opportunity to monitor a part through surface based measurements to characterise the whole volume. Many of the Non-Destructive Evaluation (NDE) approaches to gain industrial traction thus far generate optical datasets which can be used to identify surface breaking mechanical defects [8], but fail to capture information in the subsurface, where porosity is known to form through the keyhole mechanism [9].

One approach uniquely positioned to address many of the challenges posed by quality assurance in PBF is Spatially Resolved Acoustic Spectroscopy (SRAS). An acoustic microscopy technique, based on laser ultrasonics, the use of SRAS for additive manufacturing has been discussed in previous literature, and the appropriateness can be summarised by SRAS ability to detect and differentiate between surface and subsurface defects [10] and make informative measurements of the texture which can be correlated to build parameters [11].
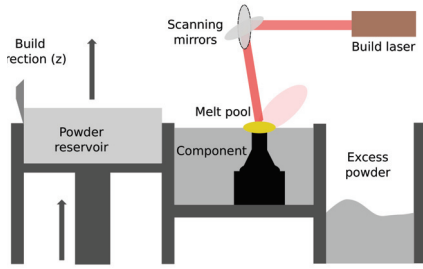
(a) Schematic of powder bed fusion process within a typical current-class build system.
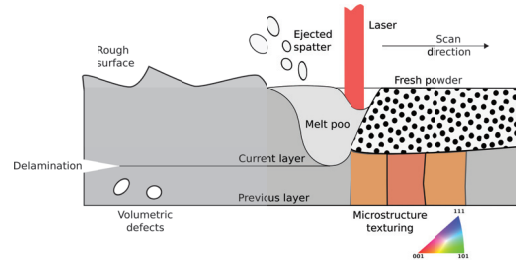
(b) Detailed illustration of melt pool phenomena in powder bed fusion.

Figure 1: Illustration of the powder bed fusion process

This study is designed to investigate the ability of SRAS to capture meaningful crystalline texture and defect information in an Inconel 718 PBF specimen.

SPATIALLY RESOLVED ACOUSTIC SPECTROSCOPY

SRAS is a non-contact, non-destructive laser ultrasonic technique, useful for probing the mechanical properties of a sample. The technique uses a broadband pulsed laser for generation, by placing an optical mask in the beam path a fringe pattern, with spacing λ_g, can be imaged on to the sample. Thermoelastic absorption of the laser energy causes rapid deformation of area under the generation, inducing a stress field and in turn causing acoustic waves to propagate. In the thermoelastic regime surface acoustic waves (SAWs) are efficiently produced, primarily the Rayleigh wave. The Rayleigh wave has the useful property of being non-dispersive, in practice this means the frequency, f_s of the wave packets stays constant along the propagation length. This allows the SAW packet to be detected at an arbitrary distance from the generation patch.

Detection of the acoustic wave is made though a second continuous-wave laser in combination with a knife edge detector (KED). By probing the the optical beam deflection at the photo-diode caused by propagation of the acoustic wave, it is possible to measure the wave frequency, f_s. Having set the acoustic wavelength, λ_g, and measured the frequency of the SAW packet, f_s, the velocity, v_s, can be calculated by Equation 1. This is unlike many laser ultrasonic techniques which rely upon time of flight measurements, making SRAS uniquely robust to aberrations and scattering effects from the microstructure [12].

$$v_s = f_s \times \lambda_g \tag{1}$$

Farnell first showed the importance of crystalline orientation on the SAW velocity [13], therefore by raster scanning in polycrystalline a sample it is possible image the microstructure contrast [14]. This phenomena has been exploited by Li et al. to allow acoustic measurements to recover crystalline orientation [15]. In large grain samples, where the grain size is much larger than the generation patch, it is possible to resolved the precise orientation of each grain. Unlike other microscopy techniques offering similar orientation information, primarily Electron Scatter Diffraction (EBSD), SRAS does not require a vacuum for operation meaning the size of sample which can be scanned is only limited in practice by the travel of translation stages. Additionally, the surface preparation required is less stringent, an arithmetic mean roughness of $R_a < 100$ nm can be considered optically smooth in this application.

The typical grain size found in as-deposited PBF components, make it infeasible to recover exact orientation of individual grains with the current instrumentation. Instead, acoustic velocity measurements are a function of the elastic properties of all grain under the generation patch, allowing the meso-scale texture to be probed.

Usefully, the secondary detection laser also allows a second distinct dataset, akin to an optical micrograph, to be captured. This dataset maps the level of light reflected from the sample to the KED. Surface breaking defects, such as porosity, present as significant drops in reflectance.

The current deployment of the SRAS technique utilises a broadband Q-switched laser (AOT-YAG-10Q), at a wavelength of 1064 nm (near-infra-red) for generation. The laser operates at a repetition rate of 2 KHz, with a pulse

width of $1-2$ ns and pulse energy of $50-150\,\mu$J. The detection laser is a low noise continuous wave laser (Cobolt Samba), at wavelength 532 nm (green), with an output power of 200 mW after fibre coupling into the optical set-up. Scanning stages (Physik Instrumente M-413 and M-414) are used to keep the optical set-up static and move the sample for raster scanning. All SRAS datasets presented in this work have been captured on prepared samples, allowing the 'smooth' surface knife-edge detector to be used, at an acoustic wavelength of $\sim 24\,\mu$m, giving a spatial resolution of $\sim 100\,\mu$m.
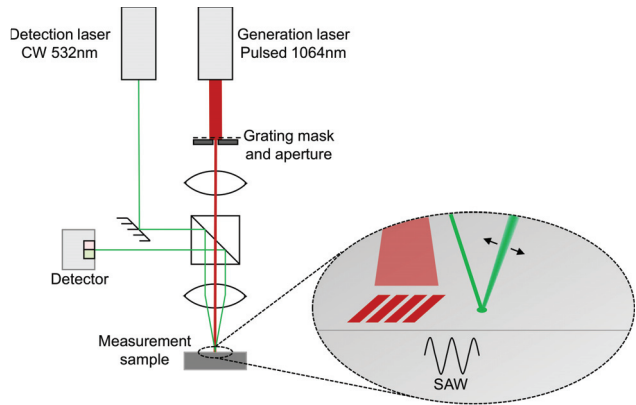
(a) Schematic of current SRAS set-up.
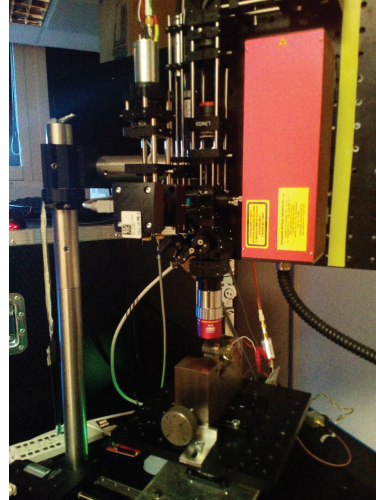
(b) Photograph of the current iteration of SRAS instrumentation, colloquially known as the EMDA system, used throughout this study.

Figure 2: Ray schematic and photograph of current SRAS instrumentation.

Smith et al. first investigated the functionality of SRAS for inspection of PBF parts, with the authors concluding the ability detect subsurface defects and possibly make useful microstructural texture measurements may address many of the challenges posed by PBF quality control [10]. This work has latterly been advanced by Hirsch et al. where meso-scale texture features and defects have been identified and correlated with build strategies [11]. Additionally, datasets generated by the SRAS technique have been used as inputs to create rework vectors, a step towards online repair [16]. The continuing ambition is to develop the instrumentation into a system appropriate for integration within a build system, in order to capture acoustic data during fabrication

MATERIALS AND METHODOLOGY

Samples have been manufactured using the common aerospace nickel super alloy Inconel 718, often favoured in gas turbine applications for its temperature, corrosion and creep resistance. The composition of the alloy is given in Table 1.

Table 1: Chemical composition of nickel-based superalloy Inconel 718 [17].

Elements	Ni	Cr	Cb	Mo	Ti	Al	Co
% wt.	53.4	18.8	5.27	2.99	1.02	0.50	0.17
Elements	Si	Mn	Cu	C	P	Fe	
% wt.	10.12	0.07	10.07	10.03	10.01	Bal	

The specimen under study was manufactured using a ReaLizer SLM50 build platform, using an island and boundary strategy with a hatch spacing of 60 μm. A laser power of 100 W and scanning speed of 560 mms^{-1} were used

to build layer thicknesses of 40 μm. Gas atomised powder sized 15–45 μm. (measured with a Malvern Mastersizer 3000) was used as the powder feedstock.

The manufactured sample was a triangular in shape, with constant cross-section and nominal height and width of 14 mm and 11.5 mm, respectively. The triangular shape was chosen to allow insight into the effect of varying scan length by geometry would have on the texture, capturing the complex effects of varying dwell time between hatch lines [18].

A schematic of the island-boundary scan pattern used is shown in Figure 3b. Upon the deposition of a new layer the laser first forms the outer boundary of the sample before progressing from the tip irradiating successive island regions individually. Thus, in effect the specimen was formed of an array of smaller squares, this can be seen clearly in Figure 3a, showing a photo of the sample in its as-deposited state after fabrication.

(a) Photograph of sample in as-deposited state. (b) Schematic of sample showing the island scan strategy.
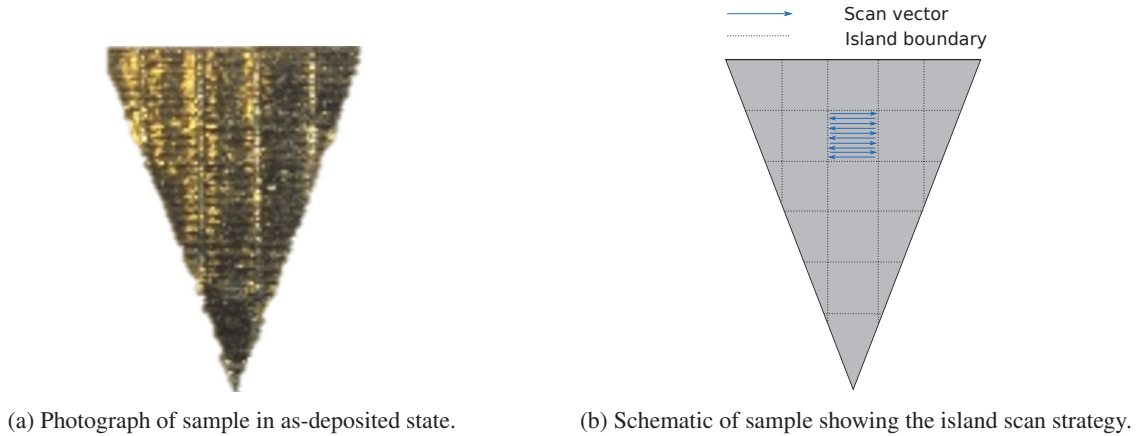
Figure 3: Sample under study in this work.

All specimens were ground and polished to give an $R_a < 20$ nm prior to inspection with the SRAS instrumentation, to allow detection of the acoustic packet by optical beam deflection and the KED.

Electron Back Scatter Diffraction (EBSD) has been used to probe the crystalline orientation of detailed sections of the sample. EBSD datasets were captured using a JEOL 7100F FEG-SEM scanning electron microscope, with Oxford Instruments EDSD system and Aztec acquisition package.

CRYSTALLOGRAPHIC TEXTURE

Figure 4 shows the (a) SAW velocity and (b) optical maps generated from the Inconel 718 triangle. Comparing the two datasets it is clear that that whilst the boundary interface between the islands cannot be discerned in the optical image, it has created a strong microstructral texture discontinuity that can be clearly observed in the velocity map. Referring back to the photograph of the sample, Figure 3a, these texture boundaries clearly correspond to the interfaces between hatched areas, the acoustic image bares a remarkable similarity to the photograph of the as-deposited sample. This is a clear exemplification of the impact varying hatching patterns can have on component microstructure. Additionally, the islands located on the perimeter of the triangle have shorter scan vectors than the bulk of the material which may be the cause of the repeated high velocity clustering within these areas. A smaller vector length will reduce the time between the melting of successive vectors, which may promote a different solidification to that seen in the bulk.

(a) SRAS velocity map of sample.

(b) SRAS optical return from sample.
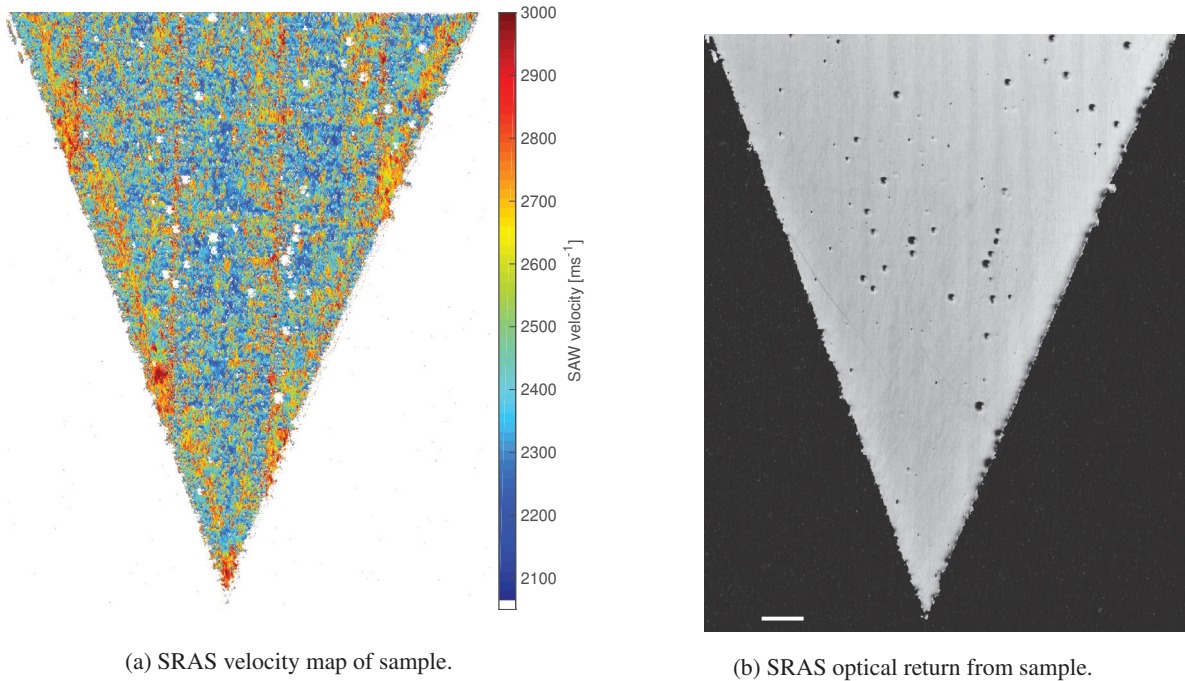
Figure 4: SRAS datasets produced from scanning of the Inconel 718 triangle sample.Scale bar shown in (b) indicated 2 mm.

Whilst useful to see the microstructural contrast provided by the velocity image it is often useful to also understand the effects on crystalline orientation. The forward problem of simulating SAW velocity as a function of crystalline plane has previously been reported by Li et al [19]. Having calculated the velocity for every propagation angle on each plane it is possible to plot the average velocity as a function of crystallographic orientation. Elastic constants for Inconel 718 are not widely available, thus simulations were performed for a number of similar nickel superalloys and pure nickel. For brevity, only pure nickel is shown in Figure 5 as this was found to be a good approximation for all nickel alloys (elastic constants from Salama and Alers [20]). In all simulated nickels, faster velocities suggested an orientation towards [001], and slower moving towards [111]. Thus from comparing Figure 5 to Figure 4a it can be said that the interface zones are closer to a [001] orientation, whilst the island areas are closer to a [111] orientation. This is in good agreement with the findings of Carter et al. [21], who used EBSD to study the influence of scanning interface regions on the formation of nickel superalloys.

To further investigate the crystallographic information contained within the SAW velocity map, EBSD imaging was carried on the sample as a comparator. Figure 6 compares the SRAS velocity map and EBSD orientation information for the tip of the triangle. The EBSD data suggested the tip of the triangle consists primarily of colonies at [001] and [101] orientation. Remembering the spatial resolution of the SRAS velocity map in question is $\sim 100 \ \mu$m, compared to the EBSD resolution of ~ 10 nm, the datasets compare well. Most notably, both suggest a strong [001] orientation
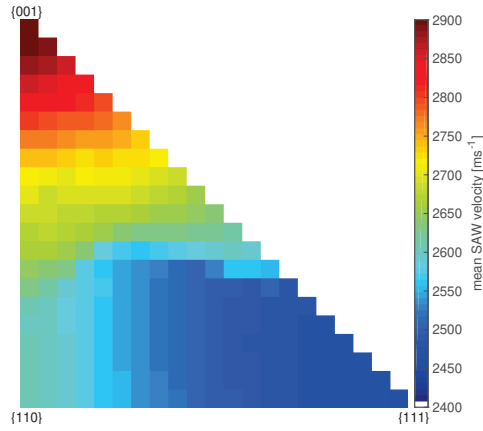
Figure 5: Mean SAW velocity as a function of orientation.

at the very tip of the triangle. Moving further up, both suggest a similar formation of [101] towards the perimeter before transitioning to [001], this may be an effect of a different cooling profile due to be being at the edge of the specimen.
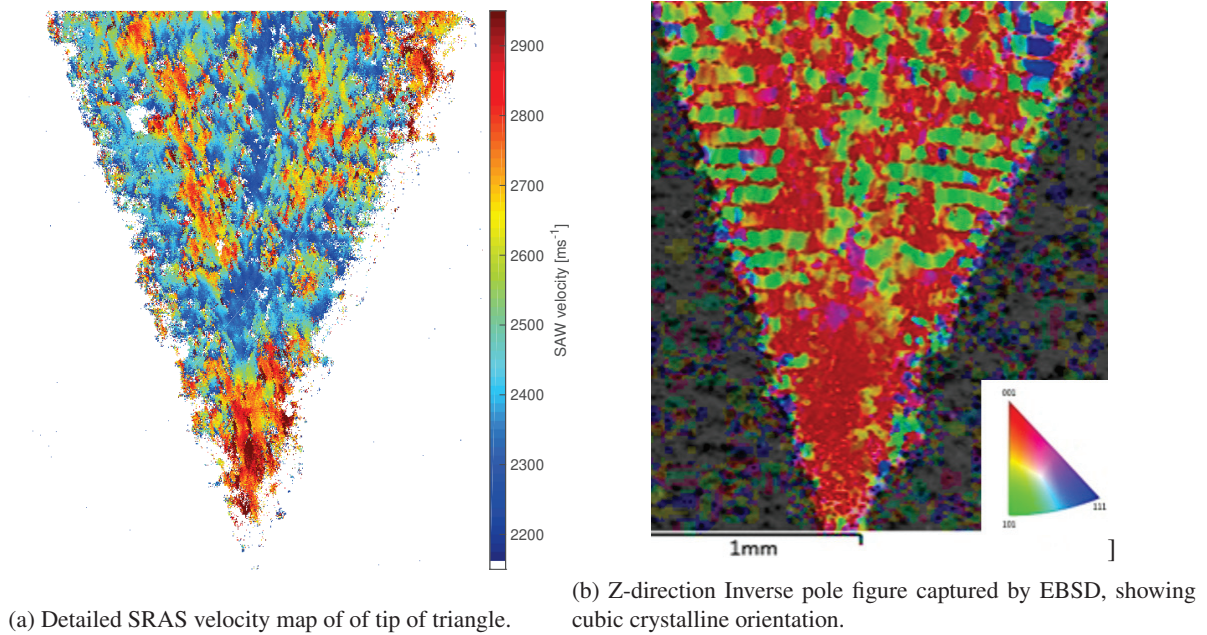
(a) Detailed SRAS velocity map of of tip of triangle.

(b) Z-direction Inverse pole figure captured by EBSD, showing cubic crystalline orientation.

Figure 6: Crystalline texture comparison in Inconel 718 triangle, by SRAS and EBSD.

Figure 7 shows the SAW velocity gradient in the sample. It is possible to equate acoustic velocity with material stiffness, simply the stiffer the sample the faster the acoustic wave shall propagate [22]. Thus, larger acoustic velocity mismatches are also suggestive of a stark stiffness interface. Under loading the rates of deformation in the scan interfaces is likely to differ significantly from the bulk of the material. It can also be seen that the interface is much stronger in the long(y) axis of the triangle, compared to the short(x) axis.
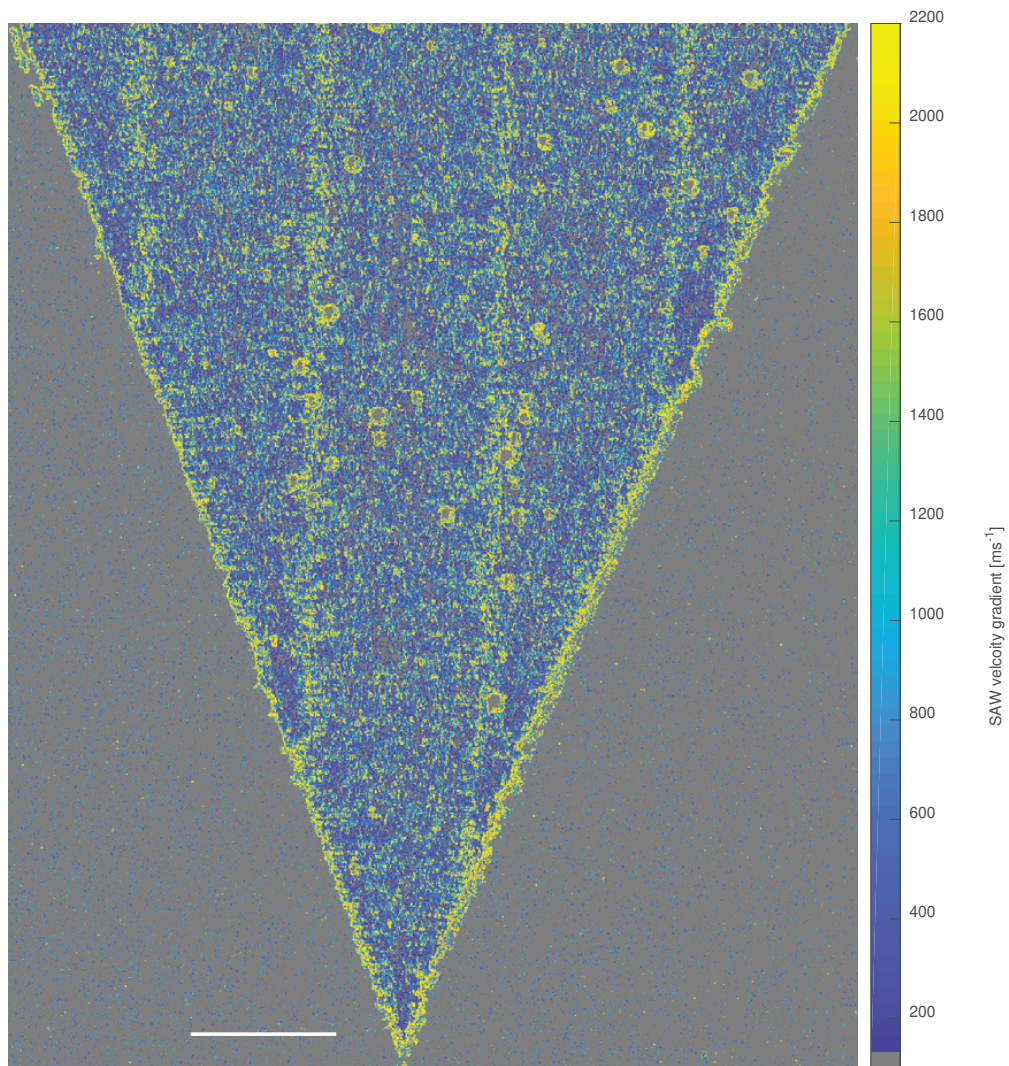
Figure 7: SAW velocity gradient in the specimen, large velocity gradients are suggestive of orientation or directional stiffness mismatches. Scale bar indicates 2 mm.

DEFECTS

The optical dataset provides useful information on the presence of surface breaking defects, Figure 4b, from this several circular pores can be identified in this specimen. Figure 8, presents (a) the area and (b) the major length of surface breaking defects in the specimen. It has previously been shown that circular defects close located close together, can combine to give excessive stress concentration factors [23]. From the optical dataset, it was found there were eight pores within the sample which have at least one unique pore located within one diameter. Under loading these features may cause premature failure.
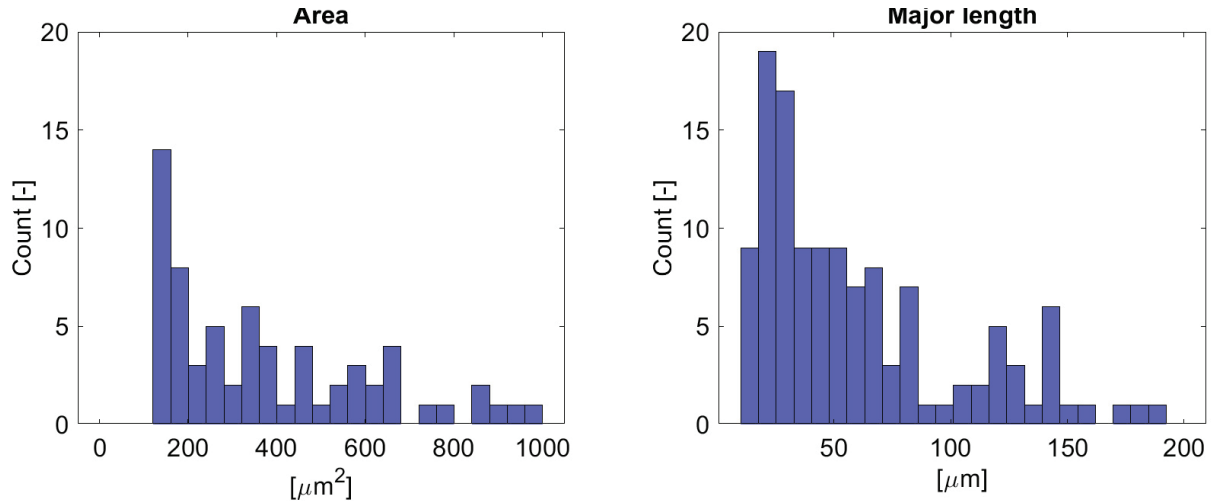
Figure 8: Histograms of surface breaking porosity area and major length, as extracted from the optical dataset.

Previous reporting has discussed the ability of SRAS to detect subsurface defects. Smith et al. found in PBF consolidated Ti-6Al-4V samples, defects located within a wavelength of the free surface were found to cause mode conversion of the customary Rayleigh wave to a Lamb plate wave. This mechanism is demonstrated in Figure 9 for the previously published titanium samples. Subsurface detection relies upon a significant shift in the phase velocity of the SAW, outside the normal range due to texture.
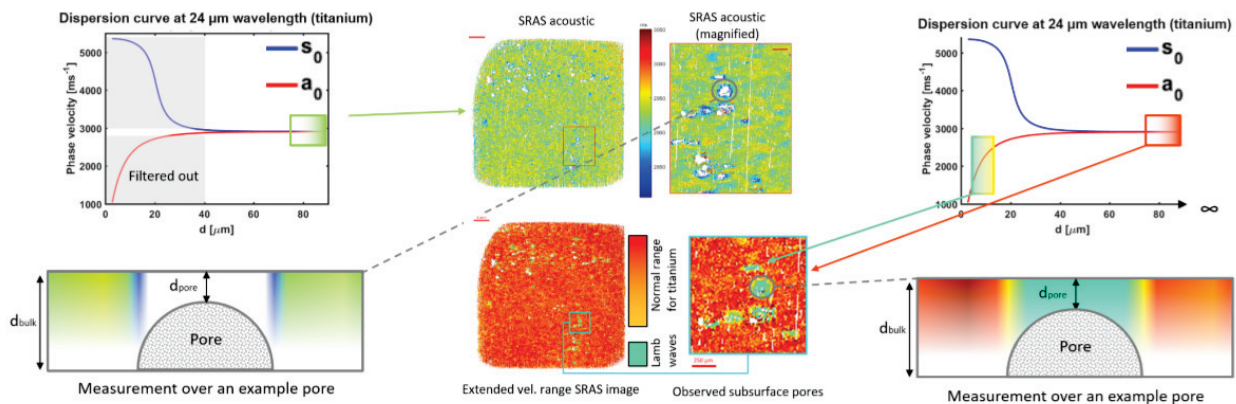
Figure 9: The mechanism for subsurface defect detection based upon Lamb wave mode conversion. In samples such as titanium with a small velocity range, subsurface features are easily distinguished from variations in the crystalline texture by the large shifts in velocity ($\sim 1000 \ ms^{-1}$.).

Interestingly, the SAW velocity maps presented in this work do not immediately suggest the presence of sub-surface defects. As discussed above, it is clear there are several surface breaking features in the studied specimen,

making it unlikely the volume was is from such defects. Instead, measurement of subsurface features is obscured due to the crystalline anisotropy of the nickel. Previous samples were fabricated in Ti-6Al-4V, which is characterised by small variations in velocity due to texture - $< 250\ ms^{-1}$ compared to the large shifts caused by Lamb wave dispersion - $\sim\ 1000\ ms^{-1}$. In contrast, a single grain in nickel can have variations of $\sim\ 1000\ ms^{-1}$, across a single plane. Figure 10 is a waterfall plot showing the fundamental anti-symmetric mode, a_0, in nickel on the (001) plane, at an inspection wavelength of 24 μm, as a function of propagation angle and media thickness. As the depth of the media approaches twice the acoustic wavelength, the velocity tends towards the normal Rayleigh wave velocity. In the case of nickel, even large shifts in velocity will often fall within the normal Rayleigh wave velocity range, meaning sub-surface defects are obscured by normal microstructural variations. One possible solution to this is vary the inspection wavelength. Textural effects should not cause the measured SAW velocity to change when scanning a different acoustic wavelengths. However, by varying the wavelength the acoustic penetration depth can be controlled, thus the shift in velocity from subsurface features varied. Thus, by scanning a multiple wavelengths it shall be possible to de-couple texture and subsurface defect effects.
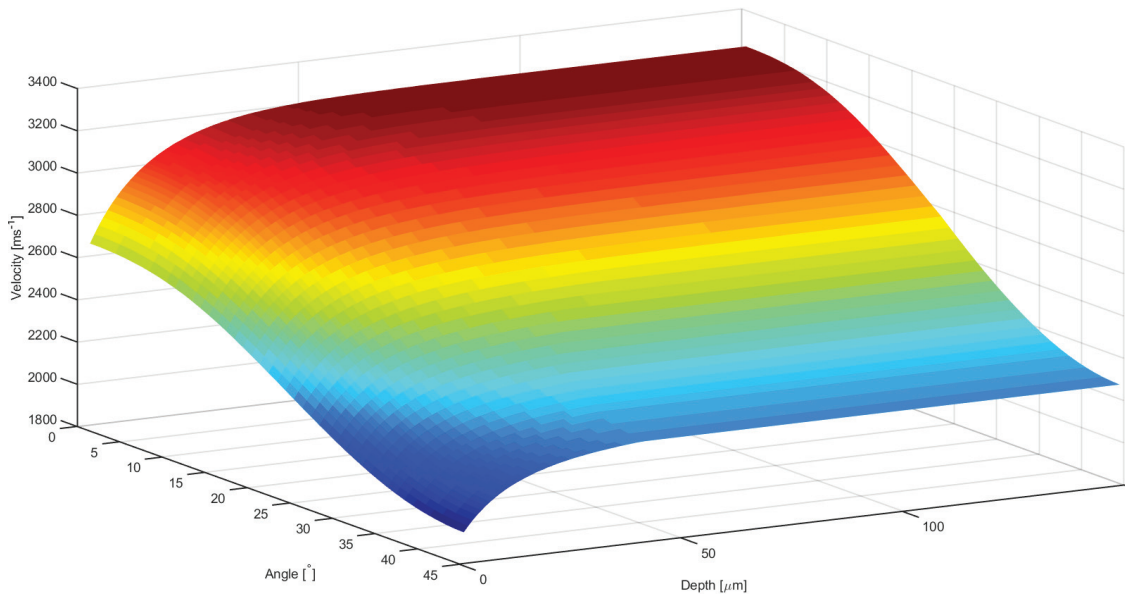
Figure 10: Fundamental anti-symmetric mode, a_o, velocity as a function of propagation angle and media thickness, on the (001) plane in pure nickel for an acoustic inspection wavelength of 24 μm. At a depth of $\sim$ 50 μm the fundamental Lamb modes converge to the Rayleigh wave velocity.

TOWARDS ONLINE MEASUREMENTS

Data presented in this work has been captured from prepared sample surfaces. The authors acknowledge the challenges accompanying a move to measuring as-deposited surfaces, which are are optically rough. The diffuse reflection from a rough surface prevents the use of the classic KED, instead other forms of optical detection which are better prepared for dealing with speckle patterns is required. Existing commercial detectors rely on approaches that either adapt to the speckle pattern, such as two-wave mixing [24] and random quadrature demodulation [25] or are inherently insensitive to speckle, Fabry-Pérot interferometry [26]. The industrial application of these techniques is often hindered by slow adaption/scanning rates. Clearly, minimising scan time is a keystone in making SRAS a viable in-situ solution to PBF inspection, necessitating the development of an alternative detector. The Speckle Knife Edge Detector (SKED) makes use of an array of photo-diodes to unravel the speckle by measuring the differences in light intensity across the detector [27]. Allowing efficient detection of the SAW, despite surface roughness. Characterisation of the SKED and imaging of as-deposited PBF samples will be reported in forthcoming literature. A final important factor for this application is the time for inspection. The EBSD data captured in this study at only the tip took $\sim$ 14 hours to acquire, whilst the

SRAS velocity map for the whole sample took ∼ 1 hour. The current SRAS instrumentation captures ≈1000 points per second, currently limited by the scanning stages and generation laser repetition rate. Hirsch et al. have previously reported on the temporal impact of an in-situ SRAS system, as a function of spatial resolution and measurement fidelity [28]. Essentially, the data capture rate of a prospective in-situ SRAS system will be limited by the repetition rate of the generation laser - the more pulses per second the faster data can be acquired.

CONCLUSION

In summary, this work has investigated the capability of SRAS to detect variations in the microstructure of a nickel superalloy specimen consolidated by powder bed fusion. The microstructural texture images were found to compare well with the corresponding EBSD imaging. The influence of the island scanning pattern could not be seen in the optical dataset but is clearly identifiable in the SAW velocity map. In fact, the acoustic map is seen to compare remarkably well with the photograph of the as-deposited sample surface. Clear variations in the texture formation were observed between the bulk of the material and the islands at the perimeter, this is thought to be a result of reduced time between successive hatches due to shorter hatch vectors at the edge of the specimen. In these area clear high velocity clustering could be discerned. These outcomes highlight both the impact of scan strategy on the texture formation of parts consolidated by PBF and more pertinently the ability of SRAS to both detect and quantify these variations.

The presence of subsurface defects was not evident in the captured SAW velocity maps, given the number of surface breaking defects found it is unlikely the bulk of the sample was fully dense. Instead, it has been suggested that the relative anisotropy of nickel and nickel-based alloys cause subsurface defects to be obscured by normal variations in velocity due to crystalline texture.

ACKNOWLEDGEMENTS

REFERENCES

[1] W. E. Frazier, "Metal additive manufacturing: A review," *Journal of Materials Engineering and Performance*, vol. 23, 2014.

[2] B. Zhang, Y. Li, and Q. Bai, "Defect formation mechanisms in selective laser melting: A review," *Chinese Journal of Mechanical Engineering*, vol. 30, no. 3, pp. 515–527, 2017.

[3] N. Shamsaei, A. Yadollahi, L. Bian, and S. M. Thompson, "An overview of direct laser deposition for additive manufacturing; part ii: Mechanical behavior, process parameter optimization and control," *Additive Manufacturing*, vol. 8, pp. 12 – 35, 2015.

[4] J. H. Martin, B. D. Yahata, J. M. Hundley, J. A. Mayer, T. A. Schaedler, and T. M. Pollock, "3d printing of high-strength aluminium alloys," *Nature*, vol. 549, pp. 365–369, Sept. 2017.

[5] A. Leicht, U. Klement, and E. Hryha, "Effect of build geometry on the microstructural development of 316l parts produced by additive manufacturing," *Materials Characterization*, vol. 143, pp. 137 – 143, 2018. Metal Additive Manufacturing: Microstructures and Properties.

[6] M. Baumers, P. Dickens, C. Tuck, and R. Hague, "The cost of additive manufacturing: machine productivity, economies of scale and technology-push," *Technological Forecasting and Social Change*, vol. 102, pp. 193 – 201, 2016.

[7] S. K. Everton, M. Hirsch, P. Stravroulakis, R. K. Leach, and A. T. Clare, "Review of in-situ process monitoring and in-situ metrology for metal additive manufacturing," *Materials and Design*, 2016.

[8] M. Grasso and B. M. Colosimo, "Process defects and in situ monitoring methods in metal powder bed fusion: a review," *Measurement Science and Technology*, vol. 28, 2017.

[9] C. Zhao, K. Fezzaa, R. W. Cunningham, H. Wen, F. De Carlo, L. Chen, A. D. Rollett, and T. Sun, "Real-time monitoring of laser powder bed fusion process using high-speed x-ray imaging and diffraction," *Scientific Reports*, vol. 7, p. 3602, June 2017.

[10] R. J. Smith, M. Hirsch, R. Patel, W. Li, A. T. Clare, and S. D. Sharples, "Spatially resolved acoustic spectroscopy for selective laser melting," *Journal of Materials Processing Technology*, 2016.

[11] M. Hirsch, S. Catchpole-Smith, R. Patel, P. Marrow, W. Li, C. Tuck, S. D. Sharples, and A. T. Clare, "Meso-scale defect evaluation of selective laser melting using spatially resolved acoustic spectroscopy," *Proc. R. Soc. A*, 2017.

[12] S. Sharples, M. Clark, and M. Somekh, "Dynamic higher-order correction of acoustic aberration due to material microstructure," *Applied Physics Letters*, vol. 81, no. 12, pp. 2288–2290, 2002.

[13] G. Farnell, *Principles and Methods, Physical Acoustic*, vol. VI. Academic Press, 1970.

[14] R. J. Smith, W. Li, J. Coulson, M. Clark, M. G. Somekh, and S. D. Sharples, "Spatially resolved acoustic spectroscopy for rapid imaging of material microstructure and grain orientation," *Measurement Science and Technology*, vol. 25, no. 5, p. 055902, 2014.

[15] W. Li, J. Coulson, J. W. Aveson, R. J. Smith, M. Clark, M. G. Somekh, and S. D. Sharples, "Orientation characterisation of aerospace materials by spatially resolved acoustic spectroscopy," *Journal of Physics: Conference Series*, vol. 520, p. 012017, 2014.

[16] M. Hirsch, P. Dryburgh, S. Catchpole-Smith, R. Patel, L. Parry, S. Sharples, I. Ashcroft, and A. Clare, "Targeted rework strategies for powder bed additive manufacture," *Additive Manufacturing*, vol. 19, pp. 127 – 133, 2018.

[17] M. Rahman, W. K. H. Seah, and T. T. Teo, "The machinability of inconel 718," *Journal of Materials Processing Technology*, vol. 63, no. 1-3, pp. 199–204, 1997.

[18] P. Karimi, T. Raza, J. Andersson, and L. Svensson, "Influence of laser exposure time and point distance on 75 micron thick layer of selective laser melted alloy 718," *Int J Adv Manuf Technol*, vol. 94, pp. 2199–2207, 2018.

[19] W. Li, S. D. Sharples, R. J. Smith, M. Clark, and M. G. Somekh, "Determination of crystallographic orientation of large grain metals with surface acoustic waves," *J Acoust Soc Am*, vol. 132, no. 2, pp. 738–45, 2012.

[20] K. Salama and G. Alers, "Third-order elastic moduli of pule nickel and some dilute copper-nickel alloys," in *IEEE Transactions on Sonics and Ultrasonics*, IEEE-Inst Electrical Electronics Engineers Inc345 E 47TH ST, New York, NY 10017-2394, 1969.

[21] L. N. Carter, C. Martin, P. J. Withers, and M. M. Attallah, "The influence of the laser scan strategy on grain structure and cracking behaviour in slm powder-bed fabricated nickel superalloy," *Journal of Alloys and Compounds*, vol. 615, pp. 338–347, 2014.

[22] A. Mark, W. Li, S. Sharpies, and P. J. Withers, "Comparison of grain to grain orientation and stiffness mapping by spatially resolved acoustic spectroscopy and ebsd," *Journal of Microscopy*, vol. 267, no. 1, pp. 89–97, 2017.

[23] S. Tammas-Williams, P. J. Withers, I. Todd, and P. B. Prangnell, "The influence of porosity on fatigue crack initiation in additively manufactured titanium components," *Scientific Reports*, vol. 7, no. 1, pp. 7308–, 2017.

[24] R. K. Ing and J. Monchalin, "Broadband optical detection of ultrasound by two wave mixing in a photorefractive crystal," *Applied Physics Letters*, vol. 59, no. 25, pp. 3233–3235, 1991.

[25] B. Pouet, S. Breugnot, and P. Clemenceau, "Robust laser ultrasonic interferometer based on random quadrature demodulation," *AIP Conference Proceedings*, vol. 820, no. 1, pp. 233–239, 2006.

[26] J. Monchalin, "Optical detection of ultrasound at a distance using a confocal fabry–perot interferometer," *Applied Physics Letters*, vol. 47, no. 1, pp. 14–16, 1985.

[27] S. D. Sharples, R. A. Light, S. O. Achamfuo-Yeboah, M. Clark, and M. G. Somekh, "The sked: speckle knife edge detector," *Journal of Physics: Conference Series*, vol. 520, p. 012004, 2014.

[28] M. Hirsch, R. Patel, W. Li, G. Guan, R. K. Leach, S. D. Sharples, and A. T. Clare, "Assessing the capability of in-situ nondestructive analysis during layer based additive manufacture," *Additive Manufacturing*, vol. 13, pp. 135–142, 2017.